

PHOTONICS Research

Ultrasensitive measurement of angular rotations via a Hermite–Gaussian pointer

BINKE XIA,¹  JINGZHENG HUANG,^{1,2}  HONGJING LI,¹ MIAOMIAO LIU,¹ TAILONG XIAO,¹ CHEN FANG,¹ AND GUIHUA ZENG^{1,3}

¹State Key Laboratory of Advanced Optical Communication Systems and Networks, Institute for Quantum Sensing and Information Processing, Shanghai Jiao Tong University, Shanghai 200240, China

²e-mail: jzhuang1983@sjtu.edu.cn

³e-mail: ghzeng@sjtu.edu.cn

Received 19 August 2022; revised 14 October 2022; accepted 14 October 2022; posted 14 October 2022 (Doc. ID 473699); published 28 November 2022

Exploring high sensitivity on the measurement of angular rotations is an outstanding challenge in optics and metrology. In this work, we employ the mn -order Hermite–Gaussian (HG) beam in the weak measurement scheme with an angular rotation interaction, where the rotation information is taken by another HG mode state completely after the post-selection. By taking a projective measurement on the final light beam, the precision of angular rotation is improved by a factor of $2mn + m + n$. For verification, we perform an optical experiment where the minimum detectable angular rotation improves $\sqrt{15}$ -fold with HG55 mode over that of HG11 mode, and achieves a sub-microradian scale of the measurement precision. Our theoretical framework and experimental results not only provide a more practical and convenient scheme for ultrasensitive measurement of angular rotations but also contribute to a wide range of applications in quantum metrology. © 2022 Chinese Laser Press

<https://doi.org/10.1364/PRJ.473699>

1. INTRODUCTION

Measuring the angular rotations with high sensitivity has an increasing interest recently, for its growing potential in a wide range of optical science and applications. For example, precise measurement of rotations plays a vital role in atom interferometer gyroscopes [1], optical tweezers [2], rotational Doppler effect [3–5], and magnetic field measurements [6]. Traditionally, the basic laser beam with Gaussian profile is incapable of taking angular rotations because it is rotational symmetry [7]. Motivated by the studies of light endowed with orbital angular momentum (OAM) [8], some related efforts are proposed to increase the sensitivity of angular rotation's measurement. But it is worth noting that the pure OAM lights like Laguerre–Gaussian (LG) beams are still rotational symmetry, and therefore quantum resources are involved for angular rotations measurement in addition, such as quantum entanglement of high OAM values [9] and NOON states in the OAM bases [10,11]. Recently, D'Ambrosio *et al.* also proposed a scheme on the rotation measurements with a microradian (μrad)-scaling sensitivity by utilizing the classical entangled formalism of OAM and polarization [12]. However, these schemes are complicated to implement, for example, quantum resources are usually difficult to generate [13,14] and fragile in noise [15], and a customized q -plate is necessary for generating OAM-polarization entangled formalism [12,16]. To explore

the more practical and simple protocol for precise measurement of angular rotations, Magaña Loaiza *et al.* have reported a weak value amplification scheme with experimental precision of 0.4° (≈ 7 mrad), where the light beam with angular Gaussian profile is employed [17].

Those previous works concentrated on the precision improvement via higher OAM values, but we find that the ultimate precision on rotation measurement is decided by the variance of OAM distribution instead of OAM value. Therefore, we employ the Hermite–Gaussian (HG) pointer to achieve an ultrahigh sensitivity on the measurement of angular rotations because of its large OAM variances. Previously, the n -order HG pointer was employed on the measurement of spatial displacement [18,19], where the corresponding quantum Cramér–Rao (QCR) bound [20] was improved linearly with mode number n . In this work, we employ the mn -order HG pointer in a rotational-coupling weak measurement scheme. After the post-selection, the information of angular rotation is taken by an HG mode state, which is orthogonal to the initial pointer state. Then projecting the final light beam to the state taking angular rotations, the quantum limit precision of rotation measurement can be achieved, which is enhanced with a factor of $2mn + m + n$.

For demonstration, we set up an optical experiment to implement the precision measurement of angular rotation. Instead of the tomography of OAM distribution in Ref. [17],

we demodulate the angular rotations from the projection intensity directly, and the imaginary weak value is also not necessary. The measurement precision in our experiment achieves $0.89 \mu\text{rad}$ with the 5×5 -order HG beam. Our results shed new light on the precise measurement of angular rotation and have potential for optical metrology, remote sensing, biological imaging, and navigation systems [4,21,22].

2. THEORETICAL MODEL

A. Enhanced Quantum Limit via HG Pointer

To be clear, we first consider the general weak measurement process with post-selection as depicted in Fig. 1. For simplicity, we consider a two-level system with initial state $|i\rangle$ and a pointer with initial state $|\psi_i\rangle$. They couple together during the weak interaction procedure with an impulse Hamiltonian $\hat{H}_I = \delta(t - t_0)\alpha\hat{A} \otimes \hat{\Omega}$, where $\hat{\Omega}$ is a translation operator on the pointer, and α is the corresponding interaction strength. Here \hat{A} is a Pauli operator on the two-level system. In weak measurement scheme, the interaction strength $\alpha \ll 1$, and then the unitary evolution operator of weak interaction procedure can be approximately calculated as $\hat{U} = \exp(-i \int \hat{H}_I dt) \approx 1 - i\alpha\hat{A} \otimes \hat{\Omega}$. (Without loss of generality, we adopt units making $\hbar = 1$ in this paper.)

To individually read out the measurement information from the pointer, we post-select the system by state $|f\rangle$ and turn the final state in whole to be $|\psi_f\rangle|f\rangle$, where $|\psi_f\rangle \approx \mathcal{N}(1 - i\alpha A_w \hat{\Omega})|\psi_i\rangle$ is the pointer's final state, and $\mathcal{N} = 1/\sqrt{1 + 2\alpha\text{Im}(A_w)\langle\hat{\Omega}\rangle_i + \alpha^2|A_w|^2\langle\hat{\Omega}^2\rangle_i}$ is the normalized factor with $\langle\hat{\Omega}\rangle_i = \langle\psi_i|\hat{\Omega}|\psi_i\rangle$, $\langle\hat{\Omega}^2\rangle_i = \langle\psi_i|\hat{\Omega}^2|\psi_i\rangle$. A_w is a weak value calculated by $A_w = \langle f|\hat{A}|i\rangle/\langle f|i\rangle$ [23,24].

To analyze the estimating precision in our weak measurement scenario, we employ the quantum Fisher information (QFI) as a figure of merit [25,26]. The QFI of final pointer state $|\psi_f\rangle$ about interaction strength parameter α can be calculated as $\mathcal{Q}(\alpha) \approx 4|A_w|^2\langle\Delta\hat{\Omega}^2\rangle_i$, where $\langle\Delta\hat{\Omega}^2\rangle_i = \langle\hat{\Omega}^2\rangle_i - \langle\hat{\Omega}\rangle_i^2$. For N classical measured samples, the variance of estimator $\hat{\alpha}$ satisfies the QCR inequality $\delta\hat{\alpha}^2 \geq 1/N\mathcal{Q}(\alpha)$, which leads to an uncertainty relation

$$\delta\hat{\alpha}^2\langle\Delta\hat{\Omega}^2\rangle_i \geq \frac{1}{4N|A_w|^2}. \quad (1)$$

In this work, we apply the weak measurement scheme to the measurement of angular rotation. Thus, the interaction strength corresponds to the rotation angle of pointer, and the translation operator $\hat{\Omega} = \hat{L}_z$ is the OAM operator. Traditionally, the laser beam with a Gaussian profile is widely

used in weak measurement, and the corresponding spatial wave function is $\psi_G(x, y) = \frac{1}{\sqrt{2\pi\sigma_0^2}} \exp\left(-\frac{x^2+y^2}{4\sigma_0^2}\right)$, where σ_0^2 is the spatial variance of the Gaussian beam. Obviously, $\langle\Delta\hat{L}_z^2\rangle_G = 0$ because of the rotational symmetry of the Gaussian beam. Thus, it is necessary to devise an appropriate pointer for rotation measurement. In addition, as revealed from Eq. (1), increasing the variance of the OAM of the pointer is beneficial for higher precision on measuring angular rotations.

For this reason, we employ the mn -order HG beam as initial pointer for the measurement of angular rotations, where m and n are the transverse mode numbers of the x component and y component, respectively. Though the mn -order HG beam takes zero-mean OAM [7], its variance of OAM distribution increases quadratically with the mode numbers

$$\langle\Delta\hat{L}_z^2\rangle_{mn} = 2mn + m + n, \quad (2)$$

which are going to be derived from the following. Then the quantum limit of rotation measurement with the mn -order HG beam is given as

$$\delta\hat{\alpha}^2 \geq \frac{1}{4N|A_w|^2(2mn + m + n)}, \quad (3)$$

which is derived from the QCR inequality (1), and the ultimate precision is improved quadratically with mode numbers m and n . Besides the improvement on the quantum limit of rotation measurement, employing HG beams also provides a more convenient way to implement the optimal measurement for demodulating angular rotations in a practical system.

B. Operator Algebra of HG Beams

In detail, we can relate the HG beams to the harmonic oscillators (HOs) here. The wave function of the HG beam is [27]

$$u_{mn}(x, y, z) = \exp\left[\frac{ik(x^2 + y^2)}{2q(z)} - i(m + n + 1)\chi(z)\right] \times \frac{\sigma_0}{\sigma(z)} \psi_{mn}\left[\frac{\sigma_0}{\sigma(z)}x, \frac{\sigma_0}{\sigma(z)}y\right], \quad (4)$$

where the three z -dependent parameters, spatial variance σ^2 , Gouy phase χ , and radius of curvature of the wavefront q , can be determined by equalities

$$\frac{1}{2\sigma^2(z)} - \frac{ik}{q(z)} = \frac{k}{b + iz}, \quad \tan \chi(z) = \frac{z}{b}, \quad (5)$$

where k is the wavenumber and b is the Rayleigh range [28]. $\psi_{mn}(x, y)$ in Eq. (4) is the 2D harmonic HG function

$$\psi_{mn}(x, y) = \frac{H_m\left(\frac{x}{\sqrt{2}\sigma_0}\right)H_n\left(\frac{y}{\sqrt{2}\sigma_0}\right)}{\sqrt{2^{m+n+1}\pi\sigma_0^2 m!n!}} \exp\left(-\frac{x^2 + y^2}{4\sigma_0^2}\right), \quad (6)$$

where H_n is the n -order Hermite polynomial.

From the view of quantum mechanics, wave function $\psi_{mn}(x, y)$ is the time-independent solution for the Schrödinger equation of 2D harmonic oscillators:

$$i\frac{\partial\psi}{\partial t} = \left[\sigma_0^2(\hat{p}_x^2 + \hat{p}_y^2) + \frac{1}{4\sigma_0^2}(\hat{x}^2 + \hat{y}^2)\right]\psi. \quad (7)$$

For eigenvalue $E_{mn} = m + n + 1$, the corresponding eigenket can be obtained as

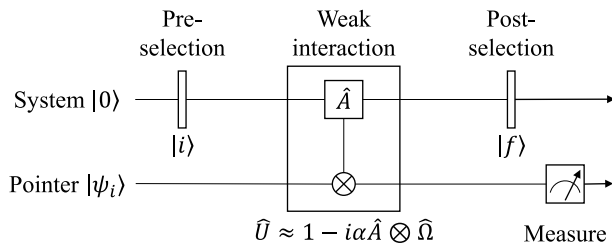


Fig. 1. Post-selected weak measurement scheme.

$$|m, n\rangle = \iint dx dy \psi_{mn}(x, y) |x, y\rangle. \quad (8)$$

Here, we denote the mn -order HG beam state as

$$|u_{mn}(z)\rangle = \iint dx dy u_{mn}(x, y) |x, y\rangle. \quad (9)$$

Obviously, $|u_{mn}(0)\rangle = |m, n\rangle$. We define the creation (annihilation) operators for the HO state $|m, n\rangle$:

$$\hat{a}_x^\dagger |m, n\rangle = \sqrt{m+1} |m+1, n\rangle, \quad \hat{a}_x |m, n\rangle = \sqrt{m} |m-1, n\rangle, \quad (10)$$

$$\hat{a}_y^\dagger |m, n\rangle = \sqrt{n+1} |m, n+1\rangle, \quad \hat{a}_y |m, n\rangle = \sqrt{n} |m, n-1\rangle. \quad (11)$$

HG beam states are z dependent, and their wave functions are the solutions of the paraxial wave equation

$$-2ik \frac{\partial}{\partial z} u(x, y, z) = \left(\frac{\partial^2}{\partial x^2} + \frac{\partial^2}{\partial y^2} \right) u(x, y, z), \quad (12)$$

which can be rewritten as

$$\frac{d}{dz} |u_n(z)\rangle = -\frac{i}{2k} (\hat{p}_x^2 + \hat{p}_y^2) |u_n(z)\rangle. \quad (13)$$

This equation has the formal solution $|u_{mn}(z)\rangle = \hat{U}(z) |u_{mn}(0)\rangle$ with the propagation operator

$$\hat{U}(z) = \exp \left[-\frac{i}{2k} (\hat{p}_x^2 + \hat{p}_y^2) z \right]. \quad (14)$$

Thus, the z -dependent mode creation (annihilation) operators can be derived by

$$\hat{a}_x(z) = \hat{U}(z) \hat{a}_x \hat{U}^\dagger(z), \quad \hat{a}_x^\dagger(z) = \hat{U}(z) \hat{a}_x^\dagger \hat{U}^\dagger(z), \quad (15)$$

$$\hat{a}_y(z) = \hat{U}(z) \hat{a}_y \hat{U}^\dagger(z), \quad \hat{a}_y^\dagger(z) = \hat{U}(z) \hat{a}_y^\dagger \hat{U}^\dagger(z). \quad (16)$$

Hence, the momentum and position operators can be obtained by these z -dependent creation and annihilation operators:

$$\begin{cases} \hat{p}_x = -\frac{i}{2\sigma_0} [\hat{a}_x(z) - \hat{a}_x^\dagger(z)] \\ \hat{x} = \sigma_0 [\hat{a}_x(z) + \hat{a}_x^\dagger(z)] + \frac{z\sigma_0}{ib} [\hat{a}_x(z) - \hat{a}_x^\dagger(z)] \\ \hat{p}_y = -\frac{i}{2\sigma_0} [\hat{a}_y(z) - \hat{a}_y^\dagger(z)] \\ \hat{y} = \sigma_0 [\hat{a}_y(z) + \hat{a}_y^\dagger(z)] + \frac{z\sigma_0}{ib} [\hat{a}_y(z) - \hat{a}_y^\dagger(z)] \end{cases}. \quad (17)$$

Moreover, it is easy to determine that the momentum operators $\hat{p}_x = -\frac{i}{2\sigma_0} (\hat{a}_x - \hat{a}_x^\dagger)$ and $\hat{p}_y = -\frac{i}{2\sigma_0} (\hat{a}_y - \hat{a}_y^\dagger)$ for 2D HO states, which have the same expression as those of HG beam states. In other words, the result of inflicting displacement on the mn -order HG beam state is the same as that of the mn -order HO state. Then we can derive the OAM operator \hat{L}_z by Eq. (17):

$$\hat{L}_z = \hat{x}\hat{p}_y - \hat{y}\hat{p}_x = i[\hat{a}_x(z)\hat{a}_y^\dagger(z) - \hat{a}_x^\dagger(z)\hat{a}_y(z)]. \quad (18)$$

Obviously, the OAM variance of the mn -order HG beam $\langle \Delta \hat{L}_z^2 \rangle_{mn} = 2mn + m + n$ is z independent, and the OAM operator \hat{L}_z is also z independent because $\hat{L}_z \equiv \hat{U}(z) \hat{L}_z \hat{U}^\dagger(z)$. Thus, the mn -order HG beam state is equivalent to the mn -order HO state in the scenario of rotation measurement.

C. Saturating Quantum Limit via Projective Measurement

Taking the initial pointer state as $|\psi_i\rangle = |m, n\rangle$, then the final pointer state can be calculated as

$$|\psi_f\rangle \approx |m, n\rangle + A_w \alpha [\sqrt{m(n+1)} |m-1, n+1\rangle - \sqrt{(m+1)n} |m+1, n-1\rangle], \quad (19)$$

where the rotation parameters are carried by an HG mode state

$$|\psi_L\rangle = \frac{1}{\sqrt{2mn+m+n}} [\sqrt{m(n+1)} |m-1, n+1\rangle - \sqrt{(m+1)n} |m+1, n-1\rangle], \quad (20)$$

which is a superposition state of pointer's adjacent modes $|m-1, n+1\rangle$ and $|m+1, n-1\rangle$.

In a complete metrological process, a classical measurement strategy is necessary for the final state to read out the unknown parameters [29]. In this case, the final estimating precision of angular rotation is evaluated by the classical Fisher information (CFI):

$$\mathcal{F}(\alpha) = \sum_{\lambda} \frac{1}{\langle \psi_f | \hat{\Pi}_{\lambda} | \psi_f \rangle} \left(\frac{\partial}{\partial \alpha} \langle \psi_f | \hat{\Pi}_{\lambda} | \psi_f \rangle \right)^2, \quad (21)$$

where $\hat{\Pi} = \{\hat{\Pi}_{\lambda} | \hat{\Pi} \geq 0, \sum_{\lambda} \hat{\Pi}_{\lambda} = \hat{\mathbb{I}}\}$ is a set of positive-operator-valued measure (POVM). Then the practical precision of angular rotation is limited by the classical Cramér–Rao (CCR) bound $\delta\hat{\alpha}^2 \geq 1/N\mathcal{F}(\alpha)$. Basically, the CCR bound of a single parameter is capable of saturating the quantum limit given by QCR inequality via devising an optimal measurement strategy [29]. For the measurement of angular rotation, the tomography of OAM distributions $\hat{\Pi}_{\text{OAM}} = \{|l\rangle\langle l| | l \in \mathbb{Z}\}$ was usually chosen as the optimal POVM traditionally [17], where $|l\rangle$ is the eigenket of the OAM operator. However, the complete tomography theoretically requires infinite projective measurements on different eigenkets $|l\rangle$ for final pointer. In our scheme with an mn -order HG pointer, a single projection for final pointer on the state $|\psi_L\rangle$ is capable of demodulating the angular rotations, and the tomography of the OAM spectrum or HG mode spectrum is no longer required. Especially, no matter how large the mode number of initial HG pointer is, the optimal POVM on the final pointer is a single projective measurement $\hat{\Pi}_{\text{HG}} = \{|\psi_L\rangle\langle\psi_L|, \hat{\mathbb{I}} - \hat{\Pi}_L\}$. Then the CFI of the rotation parameter can be calculated as $\mathcal{F}(\alpha) = 4|A_w|^2(2mn+m+n)$, which leads to the CCR bound $\delta\hat{\alpha}^2 \geq 1/4N|A_w|^2(2mn+m+n)$ saturating the corresponding QCR bound in Eq. (3). To visualize the dependency of the theoretical precision limit on the mode numbers m and n , we illustrate the CCR bound of parameter α with different mode numbers under projective measurement method in Fig. 2, where the measured number of photons is set as $N = 4.04 \times 10^7$ and the weak value is set as $A_w = \cot 5^\circ \approx 11$. Besides, we also plot the CCR bound at $m = n$ with the red line in Fig. 2, where the precision limit is improved fastest, and the dependency of the sensitivity on the factor of $2mn + m + n$ is evident.

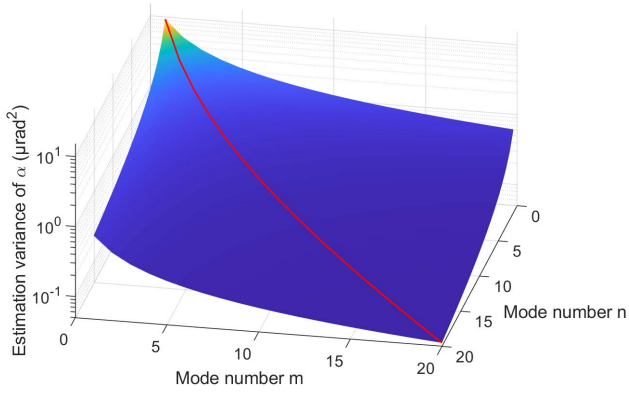


Fig. 2. Lower bound of estimation variances $\delta\hat{\alpha}^2$ with different mode numbers under the projective measurement method. The measured photons number is set as $N = 4.04 \times 10^7$, and the weak value is set as $A_w = \cot 5^\circ \approx 11$. The x axis and y axis are the mode numbers of m and n , respectively, and the z axis is the estimation variance of parameter α . The red line in this figure is the CCR bound at $m = n$, where the precision limit is improved fastest.

3. EXPERIMENTAL SCHEME

A. Experimental Materials and Setup

To experimentally verify that the enhancement on rotation measurement with an HG pointer, we setup a practical optical system to implement it as shown in Fig. 3. A light beam from a laser working at 780 nm is expanded and then converted to mn -order HG mode via a spatial light modulator (SLM) and a spatial filter system [30]. Here the beam's polarization states $|H\rangle$ and $|V\rangle$ are set as the basis of the two-level system.

We employ a Dove prism to introduce a pair of inverse weak rotations α for the $|H\rangle$ and $|V\rangle$ components in a polarizing Sagnac interferometer. The Pauli operator is denoted as $\hat{A} = |H\rangle\langle H| - |V\rangle\langle V|$. In the post-selected weak measurement scheme, pre-selection and post-selection states are nearly orthogonal to amplify the estimated parameter [17,31–35]. Thus, we choose $|i\rangle = \frac{1}{\sqrt{2}}(|H\rangle + |V\rangle)$ and $|f\rangle = \cos(\frac{\pi}{4} - \varepsilon)|H\rangle - \sin(\frac{\pi}{4} - \varepsilon)|V\rangle$, where $\varepsilon \ll 1$. Thus, the weak value $A_w = \cot \varepsilon$. Considering N measurement samples (effective measured number of photons in the experiment), the minimum detectable rotation α given by QCR bound is

$$\alpha_{\min}^{\text{QCR}} = \frac{1}{\sqrt{2}mn + m + n} \frac{1}{2|\cot \varepsilon|\sqrt{N}}, \quad (22)$$

which is significantly improved by the spatial mode numbers of the HG beams.

The laser employed in this experiment is a distributed Bragg reflector (DBR) single-frequency laser of Thorlabs Inc. (part number: DBR780PN), which works at 780 nm with 1 MHz typical linewidth. To generate the high-order HG beams, we used an SLM of Hamamatsu Photonics (part number: X13138-02), which has 1272×1024 pixels with $12.5 \mu\text{m}$ pixel pitch. The focal length of the Fourier lens in the $4f$ system is 5 cm. A $200 \mu\text{m}$ square pinhole is used as the spatial filter.

In this work, we set up a polarized Sagnac interferometer to introduce a pair of inverse rotation signals for horizontal and vertical polarization states. However, the extinction ratio of the reflection port of the polarizing beam splitter (PBS) cube (part number CCM1-PBS25-780/M of Thorlabs Inc.) is from 20:1 to 100:1 in practice, which deteriorates the degree of polarization of the output beam. Hence, we added a polarizer behind the

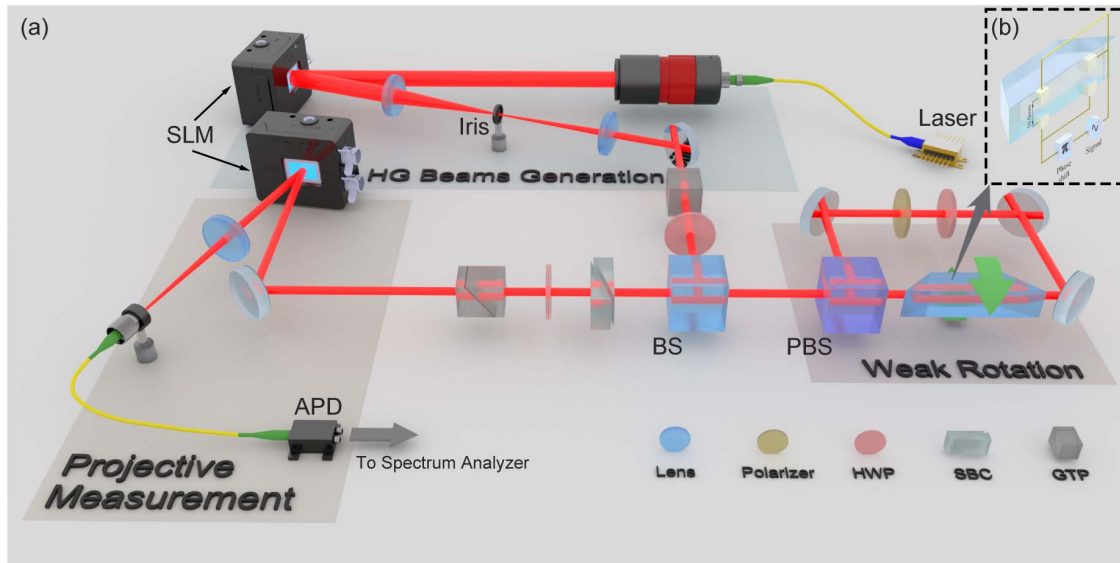


Fig. 3. Diagram of the experimental setup. (a) The mn -order HG beam is converted from an expanded Gaussian beam of an 780 nm laser by an SLM and a spatial filter system. The pre-selection is implemented by a Glan–Taylor polarizer (GTP) and an HWP. A polarized Sagnac interferometer is employed to implement the weak interaction procedure, where the inverse rotation signals are introduced by a Dove prism. Then a Soleil–Babinet compensator (SBC), an HWP, and a GTP are used to implement the post-selection. Finally, another SLM with a Fourier transfer lens is used to implement the projective measurement, where the successful projected photons are collected by an APD with an SMF. (b) Dove prism with PZT chips and generation method of the rotation signal. There are four PZT chips pasted on the reflection side of the prism with a 2×2 array, where the vertical distance of the PZT array is 10 mm.

reflection port of the PBS to improve the degree of polarization. A half-wave plate (HWP), whose optic axis is at 45° angle with respect to the horizontal plane, was employed to exchange the polarization states in the clockwise loop and counterclockwise loop.

In our experimental scheme, the Dove prism is driven by piezoelectric transducer (PZT) chips, and we exert an $f = 1$ kHz cosine driving signal on the PZT to generate the tiny rotation signal. Here, we pasted four PZT chips on the reflection side of the Dove prism as illustrated in Fig. 3(b). The four PZT chips are arranged as a 2×2 array, and the vertical distance of this array is 10 mm. Here we used the NAC2013 PZT chip of the Core Tomorrow company, which shifts 22 nm with 1 V driving voltage. We exert cosine signals (with $1/2$ amplitude DC bias) on the PZT chips, where a π -phase difference is introduced between the top-row PZT chips and bottom-row PZT chips. Therefore, a cosine driving signal with 1 V peak-to-peak voltage corresponds to a $2.2 \mu\text{rad}$ maximum rotation of the Dove prism, which leads to a $4.4 \mu\text{rad}$ transverse rotation of the input light beam. Besides this cosine driving signal, the initial rotation bias of the Dove prism, which is denoted as α_0 and on the milliradian (mrad) scale, is non-negligible. Thus, the total rotation is $\alpha_{\text{tot}} = \alpha_0 + \alpha \cos(2\pi f t)$, and it is easy to determine that $\alpha \ll \alpha_0 \ll 1$.

After the post-selection, another SLM is employed to project the final pointer to carrying state $|\psi_L\rangle$ with a Fourier transfer lens and a spatial filter from single-mode fiber (SMF) coupling detected photons to an avalanche photodiode (APD, part number: APD440A of Thorlabs Inc.), which has maximum conversion gain of 2.65×10^9 V/W and 100 kHz bandwidth. Then the detected voltage signal is analyzed by the spectrum analyzer module of Moku:Lab, which is a reconfigurable hardware platform produced by Liquid Instruments. The resolution bandwidth (RWB) of spectrum analyzer was 9.168 Hz in our experiment, which leads to the detecting time of $\tau = 109.08$ ms.

B. Experimental Results

In practice, before exerting the driving signal, we project the final pointer to state $|m, n\rangle$ to fix the measured photons number N for different HG pointers. In the experiment, the detected power of the APD is fixed as $I_0 = 94.34$ pW at the beforehand projection step. Theoretically, the detected optical power is given as $I_0 = \gamma N / \tau$, where γ is the energy of a single photon at $\lambda = 780$ nm and the detecting time duration $\tau = 109.08$ ms in our experiment. Thus, the effective measured photons number is fixed as $N = 4.04 \times 10^7$ in this experiment.

Then, exerting the driving signal on the PZT chips and projecting the final pointer to $|\psi_L\rangle$, the detected photons number is

$$\begin{aligned} N_\alpha &= |\langle \psi_L | \hat{\Pi}_L | \psi_L \rangle|^2 N = (2mn + m + n)(\cot \epsilon)^2 \alpha_{\text{tot}}^2 N \\ &\approx (2mn + m + n)(\cot \epsilon)^2 \alpha_0^2 N \\ &\quad + 2(2mn + m + n)(\cot \epsilon)^2 \alpha_0 \alpha \cos(2\pi f t) N. \end{aligned} \quad (23)$$

Similarly, the detected power of the APD is

$$\begin{aligned} I_\alpha &\approx (2mn + m + n)(\cot \epsilon)^2 \alpha_0^2 I_0 \\ &\quad + 2(2mn + m + n)(\cot \epsilon)^2 \alpha_0 \alpha \cos(2\pi f t) I_0. \end{aligned} \quad (24)$$

Inputting the detected power signal of the APD into a spectrum analyzer, the tiny rotation signal at $f = 1$ kHz is demodulated as

$$I_\alpha^{1 \text{ kHz}} = 2(2mn + m + n)(\cot \epsilon)^2 \alpha_0 \alpha I_0. \quad (25)$$

From Eq. (23), we can obtain the shot noise of APD as $\delta N_\alpha = \sqrt{N_\alpha} \approx \sqrt{2mn + m + n} |\cot \epsilon| \alpha_0 \sqrt{N}$, and the corresponding shot-noise power is

$$\delta I_\alpha = \gamma \delta N_\alpha / \tau \approx \gamma \sqrt{2mn + m + n} |\cot \epsilon| \alpha_0 \sqrt{N} / \tau. \quad (26)$$

Thus, the detected peak signal-to-noise ratio of the spectrum analyzer is

$$\text{SNR} = \frac{I_\alpha^{1 \text{ kHz}}}{\delta I_\alpha} = 2\sqrt{2mn + m + n} |\cot \epsilon| \sqrt{N} \alpha. \quad (27)$$

When $\text{SNR} = 1$, the minimum detectable rotation signal can be obtained as

$$\alpha_{\text{min}}^{(m,n)} = \frac{1}{\sqrt{2mn + m + n}} \frac{1}{2 |\cot \epsilon| \sqrt{N}}. \quad (28)$$

In practice, we detected the peak level from spectrum analyzer at 1 kHz to demodulate the amplitude of rotation signal. Generally, the peak level consists of three parts: signal level, shot-noise floor, and electrical-noise floor, which is denoted as $V_p = V_\alpha + V_{\text{sn}} + V_{\text{en}}$. Here, $V_\alpha \propto I_\alpha^{(1 \text{ kHz})}$ is the signal level, $V_{\text{sn}} \propto \delta I_\alpha$ is the shot-noise level, and they vary with the different HG modes. In our experiment, the electrical noise level $V_{\text{en}} = 35.75 \mu\text{V}$ is a constant value in the experiment, which was detected without inputting light on the APD. The detected level of the total noise floor with a mn -order HG beam is $V_{\text{noise}}^{(m,n)} = V_{\text{sn}}^{(m,n)} + V_{\text{en}}$. Thus, the detected signal-to-noise ratio with a mn -order HG beam in our scheme is obtained as

$$\text{SNR}^{(m,n)} = \frac{V_\alpha^{(m,n)}}{V_{\text{sn}}^{(m,n)}} = \frac{V_p^{(m,n)} - V_{\text{noise}}^{(m,n)}}{V_{\text{noise}}^{(m,n)} - V_{\text{en}}}. \quad (29)$$

To determine the detected noise levels, we illustrate the electrical spectra of HG11 to HG66 modes at 500 Hz to 5 kHz with driving voltage 5 V in Fig. 4.

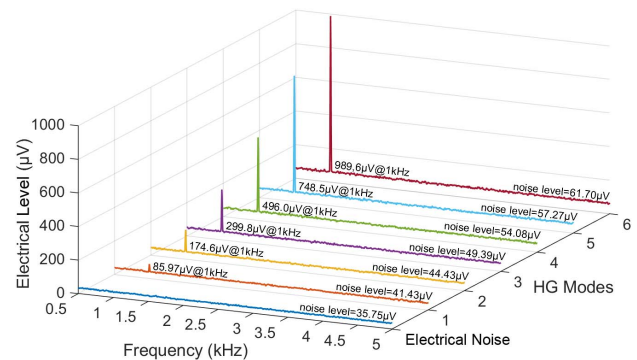


Fig. 4. Detected electrical spectrum of HG11 to HG66 modes at 500 Hz to 5 kHz. The driving voltage of the PZT is 5 V, which corresponds to $22 \mu\text{rad}$ rotation signal. The first line is the spectrum of the electrical-noise floor of the APD detector, which is detected without input light on the APD.

Table 1. Experimental Results of Detected Noise Levels

HG mode	HG11	HG22	HG33	HG44	HG55	HG66
Noise level ^a	41.43 μV	44.43 μV	49.39 μV	54.08 μV	57.27 μV	61.70 μV
Shot-noise level	5.68 μV	8.68 μV	13.64 μV	18.33 μV	21.52 μV	25.95 μV

^aTotal detected noise levels in the APD.

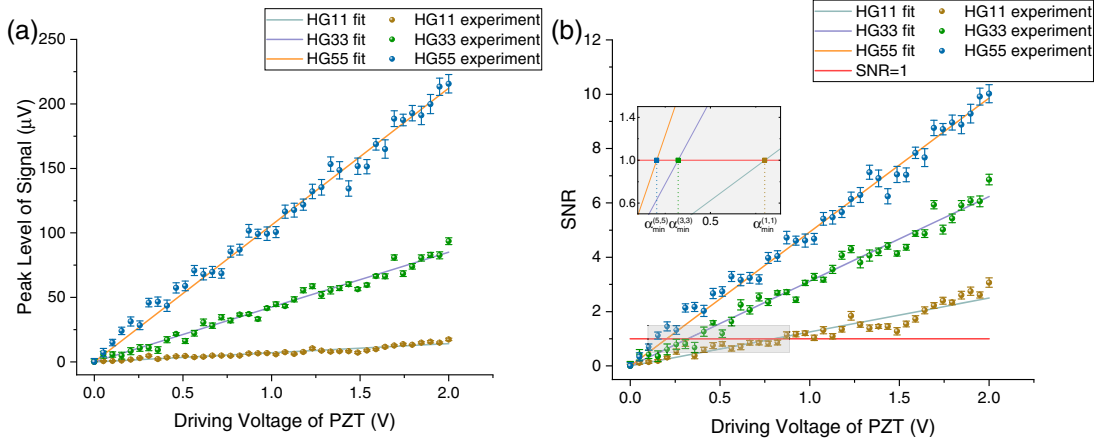


Fig. 5. Experimental results. (a) Detected peak signal level of the HG11, HG33, and HG55 modes at 1 kHz. (b) Detected signal-to-noise ratio of the HG11, HG33, and HG55 modes. The driving voltage of the PZT increases from 0 to 2 V, which corresponds to 0–8.8 μrad rotation signal.

Table 2. Minimal Detectable Rotation Angles with Different HG Modes

HG Mode	Theory ^a	Experiment	
	$\alpha_{\min}^{\text{th}}$	V_{PZT}^b	$\alpha_{\min}^{\text{exp}}$
HG11	3.44 μrad	801 mV	3.52 μrad
HG33	1.40 μrad	321 mV	1.41 μrad
HG55	0.89 μrad	203 mV	0.89 μrad

^aThese theoretical predictions are derived from Eq. (28) with fixed detected photon number $N = 4.04 \times 10^7$ and post-selection angle $\varepsilon = 5^\circ$.

^bThe driving voltages of PZT chips at SNR = 1.

As is shown in Fig. 4, the electrical noise is $V_{\text{en}} = 35.75 \mu\text{V}$, and the detected shot-noise level of the mn -order HG beam can be calculated by $V_{\text{sn}}^{(m,n)} = V_{\text{noise}}^{(m,n)} - V_{\text{en}}$. We list the results in Table 1.

In Fig. 5, we illustrate the experimental results of detected peak signal level and signal-to-noise ratio at 1 kHz with 1×1 -order, 3×3 -order, and 5×5 -order HG modes. Finally, a significant precision of 0.89 μrad is achieved with the HG55 mode in this experiment. We list the experimental results of the driving voltages of the PZT at SNR = 1 and the corresponding minimal detected rotation angles in Table 2. For comparison, we also calculate the theoretical predictions of minimal detectable rotations based on Eq. (28) with fixed detected photon number $N = 4.04 \times 10^7$ and post-selection angle $\varepsilon = 5^\circ$. Our experiment results are well consistent with the theoretical predictions.

4. DISCUSSION

A. Technical Advantages of a Weak Value

In the theoretical frame, the post-selection is employed for individually reading out the measurement parameters from the pointer, and the precision enhancement comes from the mode entanglement of the HG pointer, but not the weak values. Thus, our main conclusion still holds in the post-selection-free scheme. In the experimental scheme, we still employed the weak value amplification technology, though the weak value $A_w = \cot \varepsilon$ takes no enhancement for the theoretical minimum detectable rotation in Eq. (28) because the detected number of photons $N = |\langle f|i \rangle|^2 N_0 = \sin^2 \varepsilon N_0$ is attenuated by the post-selection, where N_0 is the number of photons before post-selection. However, the weak value amplification technology has been proved efficient for suppressing technical noises, such as reflection of optical elements [35] and detector saturation [36,37]. The detector saturation is non-negligible in our experiment since the saturation power of our APD detector is only 1.54 nW. Considering the projection demodulation of SLM, only 10% of photons can be modulated on the first-order diffraction, so the maximum efficient received power of our detector is about 154 pW, which is easily saturated without post-selection. For example, the efficient detected light power in our experiment is $I_0 = 94.34 \text{ pW}$, and the post-selection angle $\varepsilon = 5^\circ$. Therefore, for the post-selection-free scheme, an $I_0/\sin^2 \varepsilon = 12.42 \text{ nW}$ detected light power is needed to achieve the same precision of the post-selected scheme, which is far larger than the saturation power of the APD detector.

B. Rotation-Coupling Weak Measurement for Hamiltonian Estimation

Though we only investigate the enhanced measurement on angular rotation, the precision enhancement of employing HG pointers can be applied in various missions in quantum physics. The most obvious application of our scheme in quantum physics is the estimation of Hamiltonian [38,39]. In this case, we do not only concentrate on the interaction strength parameter α but we are also interested in the information of operator \hat{A} . For a two-level system, the unknown operator can be represented as $\hat{A} = \vec{n} \cdot \vec{\sigma}$, where $\vec{n} = (\sin \theta \cos \phi, \sin \theta \sin \phi, \cos \theta)$ is the direction vector of the measurement operator, and $\vec{\sigma} = (\hat{\sigma}_x, \hat{\sigma}_y, \hat{\sigma}_z)$, where $\hat{\sigma}_x$, $\hat{\sigma}_y$, and $\hat{\sigma}_z$ are Pauli matrices. Thus, there are two unknown parameters θ and ϕ to be estimated for identifying the operator \hat{A} . As we calculated in the theoretical model, the final pointer's state in our post-selected scheme is $|\psi_f\rangle \approx \mathcal{N}(1 - i\alpha A_w \hat{\Omega})|\psi_i\rangle$. Then the QFI of parameter $g \in (\theta, \phi)$ can be calculated as $\mathcal{Q}(g) \approx 4\alpha^2 |\partial_g A_w|^2 \langle \Delta \hat{\Omega}^2 \rangle_i$. Combined with the QCR inequality $\delta \hat{g}^2 \geq 1/N \mathcal{Q}(g)$, the estimation precision of parameter $g \in (\theta, \phi)$ satisfies the uncertainty relation

$$\delta \hat{g}^2 \langle \Delta \hat{\Omega}^2 \rangle_i \geq \frac{1}{4N\alpha^2 |\partial_g A_w|^2}, \quad (30)$$

where the quantum limits of Hamiltonian parameters are still governed by the variance of the translation operator on the initial pointer. This means that our scheme has potential to be applied in this scenario for improving the performance of Hamiltonian estimation. For example, the initial pointers with Gaussian profile are employed traditionally, and the two-level system couples with the pointer via a displacement interaction $\hat{\Omega} = \hat{p}_x$. Then the variances $\langle \Delta \hat{\Omega}^2 \rangle_i = \langle \Delta \hat{p}_x^2 \rangle_G = 1/4\sigma_0$, and the corresponding quantum limit on estimating Hamiltonian parameters $g \in (\theta, \phi)$ is given by

$$\delta \hat{g}^2 \geq \frac{\sigma_0^2}{N\alpha^2 |\partial_g A_w|^2}. \quad (31)$$

If we replace the Gaussian pointer by an mn -order HG pointer, the quantum limit will be improved to

$$\delta \hat{g}^2 \geq \frac{\sigma_0^2}{(2m+1)N\alpha^2 |\partial_g A_w|^2} \quad (32)$$

because the variance $\langle \Delta \hat{p}_x^2 \rangle_{mn} = (2m+1)/4\sigma_0$ increases linearly with the HG mode m in the corresponding displacement direction. Further, replacing the displacement interaction by rotational interaction, that is, $\hat{\Omega} = \hat{L}_z$, there will be a significant improvement in the precision limit on estimating Hamiltonian parameters:

$$\delta \hat{g}^2 \geq \frac{1}{4(2mn+m+n)N\alpha^2 |\partial_g A_w|^2}, \quad (33)$$

which is quadratically improved by the HG mode numbers m and n . Moreover, the enhancement factor $2mn+m+n$ is analog to the Heisenberg scaling limit in quantum interference [40] because the mode number m in the x direction and mode number n in the y direction are independent for an HG beam state or a 2D HO state. Thus, mode state $|m, n\rangle$ can be

regarded as an eigenket in the product Hilbert space $\mathcal{H}_x \otimes \mathcal{H}_y$, where \mathcal{H}_x and \mathcal{H}_y are the Hilbert spaces for the mode state in the x direction and the mode state in the y direction. Therefore, the OAM operator $\hat{L}_z = i(\hat{a}_x \hat{a}_y^\dagger - \hat{a}_x^\dagger \hat{a}_y)$ in this product Hilbert space $\mathcal{H}_x \otimes \mathcal{H}_y$, which leads to the unknown parameters (α, θ, ϕ) taken by the state $|\psi_L\rangle$. Moreover, it is obvious to note that the state $|\psi_L\rangle$ in Eq. (20) is a mode-entangled state in the product Hilbert space $\mathcal{H}_x \otimes \mathcal{H}_y$.

C. Rotation-Coupling Weak Measurement for Monitoring the Quantum Bit

Besides Hamiltonian estimation, our precision-enhanced method also has the potential for monitoring the quantum bit, which is a vital mission in quantum metrology [41]. Generally, the state of an arbitrary quantum bit (qubit) can be represented as

$$|\text{qubit}\rangle = \cos \frac{\theta}{2} |0\rangle + e^{i\phi} \sin \frac{\theta}{2} |1\rangle, \quad (34)$$

where θ and ϕ are the azimuthal angles on the Bloch sphere, and $|0\rangle$ and $|1\rangle$ are the eigenkets of Pauli operator $\hat{\sigma}_z$. To avoid apparent disturbance on the qubit, a series of continuous weak measurements is adopted to monitor it [42].

As is illustrated in Fig. 6, an ancillary device (pointer) is employed to monitor the quantum system via a weak interaction procedure, which is described by the von Neumann measurement theory [23] via an impulse Hamiltonian (here we take the monitoring of qubits on the basis of $\hat{\sigma}_z$, for example):

$$\hat{H}_I = \delta(t - t_0) \alpha \hat{\sigma}_z \otimes \hat{\Omega}, \quad (35)$$

which leads to a composite unitary evolution $\hat{U} = \exp(-i \int \hat{H}_I dt) \approx 1 - i\alpha \hat{\sigma}_z \otimes \hat{\Omega}$ of the quantum system and pointer. After the weak interaction, the measurement information of the Pauli operator $\hat{\sigma}_z$ on the qubit is transferred to the pointer shift of the ancillas via a translation operator $\hat{\Omega}$, and the final state of the whole system is

$$|\Psi_f\rangle = \cos \frac{\theta}{2} |0\rangle |\psi_+\rangle + e^{i\phi} \sin \frac{\theta}{2} |1\rangle |\psi_-\rangle, \quad (36)$$

where $|\psi_+\rangle = \exp(-i\alpha \hat{\Omega})|\psi_i\rangle$ and $|\psi_-\rangle = \exp(i\alpha \hat{\Omega})|\psi_i\rangle$. Unlike our post-selected weak measurement scheme, post-selection of the qubit is forbidden. Thus, we should measure

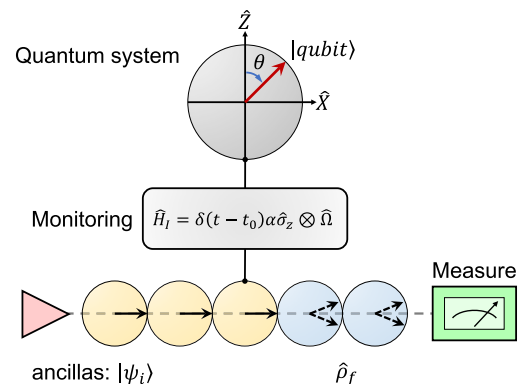


Fig. 6. Schematic of monitoring quantum bits.

the information about parameter θ from the final pointer state, which is a mixed state:

$$\hat{\rho}_f = \cos^2 \frac{\theta}{2} |\psi_+\rangle\langle\psi_+| + \sin^2 \frac{\theta}{2} |\psi_-\rangle\langle\psi_-|, \quad (37)$$

and then the corresponding QFI of parameter θ can be calculated as $\mathcal{Q}(\theta) = 1 - (\text{Re}\langle\psi_+|\psi_-\rangle)^2 \approx 4\alpha^2 \langle\hat{\Omega}^2\rangle_i$, which leads to the quantum limit on measuring parameter θ being governed by the uncertainty relation (see Appendix B for derivation)

$$\delta\hat{\theta}^2 \langle\hat{\Omega}^2\rangle_i \geq \frac{1}{4\alpha^2 N}, \quad (38)$$

which means that the monitoring sensitivity is still dependent on the devising of the pointer and coupling method. Applying our mn -order HG pointer and rotation-coupling method to this scheme, the quantum limit on monitoring the azimuthal angle θ of the qubit is then derived as

$$\delta\hat{\theta}^2 \geq \frac{1}{4\alpha^2 (2mn + m + n)N}, \quad (39)$$

where the precision enhancement still holds.

Moreover, we express the HG beams via harmonic oscillator model, which has been widely used in quantum computation and metrology topics, such as superconducting qubits [43,44] and optomechanics [45–47]. Thus, our theoretical model can be applied in such scenarios naturally and can provide a significant method in quantum metrology.

5. CONCLUSION

In summary, we have implemented a practical scheme for measuring the tiny rotation by employing an mn -order HG pointer in a post-selected weak measurement scheme, where the precision limit is theoretically improved by a factor of $2mn + m + n$. Experimentally, we demodulate the angular rotation parameter via a single projective measurement, and precision up to $0.89 \mu\text{rad}$ is achieved with 5×5 -order HG beams. Moreover, we have found that the precision enhancement of the rotation-coupling method with an HG pointer still holds in a wide range of applications in quantum physics, such as Hamiltonian estimation and monitoring qubits. Thus, our results constitute valuable resources not only for measurement and control of light's angular rotation in optical metrology but also for sensitive estimating and control of evolution procedure in quantum physics.

APPENDIX A: DERIVATION OF QUANTUM LIMITS IN A POST-SELECTED WEAK MEASUREMENT SCHEME

In this section, we give the calculation details about the quantum limits of weak interaction parameters α , θ , and ϕ in post-selection weak measurement, where α is the weak interaction strength and $\alpha \ll 1$, θ and ϕ are the Hamiltonian parameters of the two-level system. In this case, the operator \hat{A} is given as the generalized formalism $\hat{A} = \vec{n} \cdot \vec{\sigma}$, $\vec{\sigma} = (\hat{\sigma}_x, \hat{\sigma}_y, \hat{\sigma}_z)$, where $\hat{\sigma}_x$, $\hat{\sigma}_y$, and $\hat{\sigma}_z$ are the Pauli matrices. The weak interaction procedure described by an impulse Hamiltonian is

$\hat{H}_I = \delta(t - t_0)\alpha\hat{A} \otimes \hat{\Omega}$, and then the evolution operator of the weak interaction procedure can be calculated as

$$\begin{aligned} \hat{U} &= \exp(-i\hat{H}_I dt) = \exp(-i\alpha\hat{A} \otimes \hat{\Omega}) \\ &= \frac{1}{2}(\hat{I} + \vec{n} \cdot \vec{\sigma}) \exp(-i\alpha\hat{\Omega}) + \frac{1}{2}(\hat{I} - \vec{n} \cdot \vec{\sigma}) \exp(i\alpha\hat{\Omega}) \\ &\approx 1 - i\alpha\vec{n} \cdot \vec{\sigma} \otimes \hat{\Omega}. \end{aligned} \quad (A1)$$

The initial state of the whole system before weak interaction can be denoted as $|\Psi_i\rangle = |\psi_i\rangle|i\rangle$. Then the final state of the whole system after weak interaction and post-selection can be calculated as

$$\begin{aligned} |\tilde{\Psi}_f\rangle &= |f\rangle\langle f|\hat{U}|\Psi_i\rangle \approx |f\rangle\langle f|(1 - i\alpha\vec{n} \cdot \vec{\sigma} \otimes \hat{\Omega})|\Psi_i\rangle \\ &= [(\langle f|i\rangle)(1 - iM_w\hat{\Omega})|\psi_i\rangle] \otimes |f\rangle. \end{aligned} \quad (A2)$$

Here we denote $\alpha A_w = M_w$ for simplicity. Then the pointer's final state is expressed as $|\tilde{\psi}_f\rangle = \langle f|i\rangle(1 - \frac{i}{\hbar}M_w\hat{\Omega})|\psi_i\rangle$, which can be normalized as

$$|\psi_f\rangle = \mathcal{N}(1 - iM_w\hat{\Omega})|\psi_i\rangle, \quad (A3)$$

where

$$\mathcal{N} = \frac{1}{\sqrt{1 + 2\text{Im}(M_w)\langle\hat{\Omega}\rangle_i + |M_w|^2\langle\hat{\Omega}^2\rangle_i}} \quad (A4)$$

is the normalized factor.

For a parameterized state $|\psi(g)\rangle$, its corresponding QFI for a single parameter g can be given by [26,29]

$$\mathcal{Q}(g) = 4 \left[\frac{\partial\langle\psi(g)|}{\partial g} \frac{\partial|\psi(g)\rangle}{\partial g} - \frac{\partial\langle\psi(g)|}{\partial g} |\psi(g)\rangle \langle\psi(g)| \frac{\partial|\psi(g)\rangle}{\partial g} \right]. \quad (A5)$$

Substituting $|\psi_f\rangle$ into Eq. (A5), the QFI of each measurement parameter can be calculated as

$$\begin{aligned} \mathcal{Q}(g) &= 4\mathcal{N}^2 \left[\left| \frac{\partial M_w}{\partial g} \right|^2 \langle\hat{\Omega}^2\rangle_i - \mathcal{N}^2 \left(\left| \frac{\partial M_w}{\partial g} \right|^2 \langle\hat{\Omega}\rangle_i^2 \right. \right. \\ &\quad \left. \left. + \text{Im}M_w \left| \frac{\partial M_w}{\partial g} \right|^2 \langle\hat{\Omega}\rangle_i \langle\hat{\Omega}^2\rangle_i + |M_w|^2 \left| \frac{\partial M_w}{\partial g} \right|^2 \langle\hat{\Omega}^2\rangle_i^2 \right) \right] \\ &\approx 4 \left| \frac{\partial M_w}{\partial g} \right|^2 \langle\Delta\hat{\Omega}^2\rangle_i, \end{aligned} \quad (A6)$$

where $g \in (\alpha, \theta, \phi)$. Utilizing the quantum Cramér–Rao (QCR) inequality $\delta\hat{g}^2 \geq 1/N\mathcal{Q}(g)$, a coupling-parameter uncertainty relation can be obtained as

$$\delta\hat{g}^2 \langle\Delta\hat{\Omega}^2\rangle_i \geq \frac{1}{4N} \cdot \frac{1}{|\partial_g M_w|^2}. \quad (A7)$$

Note that this result is derived under the approximate condition $M_w \ll 1$.

Taking $\vec{n} = (\sin \theta \cos \phi, \sin \theta \sin \phi, \cos \theta)$, we can calculate

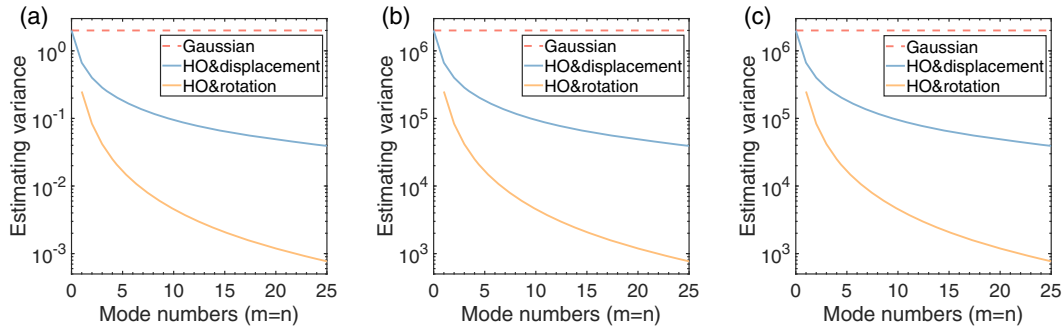


Fig. 7. QCR bounds of the measurement parameters. (a) QCR bounds of parameter α . (b) QCR bounds of parameter θ . (c) QCR bounds of parameter ϕ . The y axis is the variance of estimator \hat{g} , and the x axis is the mode numbers. Mode numbers m and n simultaneously increase from 0 to 25. The red dotted line is the QCR bound of the Gaussian pointer with displacement coupling. The blue line is the QCR bound of the HO pointer with displacement coupling. The orange line is the QCR bound of the HO pointer with rotation coupling. Here the pre-selection state and post-selection state are chosen as $|i\rangle = |f\rangle = \frac{1}{\sqrt{2}}(|0\rangle + e^{i\frac{\pi}{4}}|1\rangle)$, and values of all the parameters are $\alpha = 0.001$, $\theta = \pi/4$, and $\phi = 0$. In addition, the value of σ_0 is normalized to $1/\sqrt{2}$.

$$\begin{cases} \frac{\partial M_w}{\partial \alpha} = \sigma_{xw} \sin \theta \cos \phi + \sigma_{yw} \sin \theta \sin \phi + \sigma_{zw} \cos \theta \\ \frac{\partial M_w}{\partial \theta} = \alpha(\sigma_{xw} \cos \theta \cos \phi + \sigma_{yw} \cos \theta \sin \phi - \sigma_{zw} \sin \theta) \\ \frac{\partial M_w}{\partial \phi} = \alpha(\sigma_{yw} \sin \theta \cos \phi - \sigma_{xw} \sin \theta \sin \phi) \end{cases} \quad (\text{A8})$$

where σ_{xw} , σ_{yw} , and σ_{zw} are the corresponding weak values of Pauli operators $\hat{\sigma}_x$, $\hat{\sigma}_y$, and $\hat{\sigma}_z$, respectively. Then, substituting Eqs. (A6) and (A8) into the uncertainty relation in the inequality (A7), the lower bounds for $\delta\hat{\alpha}^2$, $\delta\hat{\theta}^2$, and $\delta\hat{\phi}^2$ can be calculated separately.

In this work, we investigate two types of pointer in the weak measurement scheme, a Gaussian pointer and an HG pointer. For the Gaussian pointer, the measurement parameters are coupled to the pointer's spatial displacement, which leads to a constant QCR bound. For the HG pointer, its mode numbers in the x direction and y direction are respectively m and n , and the QCR bound is improved with pointer's mode numbers m and n . Moreover, the 2D HG pointer theoretically equals a 2D harmonic oscillator (HO), which has been proved in the main text. Therefore, our results can be extended to any HO-formalism pointer here. Coupling the measurement parameters to the pointer's displacement (x direction), the QCR bound is improved by factor $1/(2m+1)$, which is enhanced linearly. Coupling the measurement parameters to the pointer's rotation, the QCR bound is improved by factor $1/(2mn+m+n)$, which is enhanced quadratically. Here we calculate these three QCR bounds for parameters α , θ , and ϕ at $\alpha = 0.001$, $\theta = \pi/4$, and $\phi = 0$, respectively. Without loss of generality, we normalize the value of pointer's spatial uncertainty σ to $1/\sqrt{2}$ and set the measured samples number $N = 1$. In Fig. 7, we illustrate the results for α , θ , and ϕ by choosing $|i\rangle = |f\rangle = \frac{1}{\sqrt{2}}(|0\rangle + e^{i\frac{\pi}{4}}|1\rangle)$, which equals a part measurement of the pointer without post-selection. Here $|0\rangle$ and $|1\rangle$ are the eigenkets of the Pauli operator $\hat{\sigma}_z$ on the two-level system.

In practice, the post-selection state is usually nearly orthogonal to the pre-selection state in a weak measurement scheme. Here we also analyze the impact of the post-selection state's angle. The pre-selection state is still $|i\rangle = \frac{1}{\sqrt{2}}(|0\rangle + e^{i\frac{\pi}{4}}|1\rangle)$,

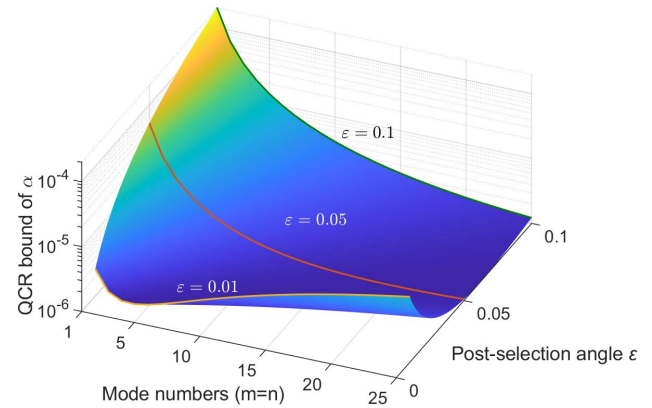


Fig. 8. QCR bound of α about post-selection angle ϵ . This is the QCR bound of α with a 2D HO pointer and rotation coupling. The x axis is the mode numbers m and n , which simultaneously increase from 1 to 25. The pre-selection state is $|i\rangle = \frac{1}{\sqrt{2}}(|0\rangle + e^{i\frac{\pi}{4}}|1\rangle)$, and the post-selection state is $|f\rangle = \frac{1}{\sqrt{2}}(|0\rangle - e^{i(\frac{\pi}{4}+\epsilon)}|1\rangle)$, where the angle ϵ varies from 0.1 to 0.01. In addition, we plot three QCR bounds at different values of ϵ . The green line is $\epsilon = 0.1$, the red line is $\epsilon = 0.05$, and the yellow line is $\epsilon = 0.01$.

and post-selection state is chosen as $|f\rangle = \frac{1}{\sqrt{2}}(|0\rangle - e^{i(\frac{\pi}{4}+\epsilon)}|1\rangle)$, where $\epsilon \ll 1$. To hold the approximate condition $M_w \ll 1$, we also require $\alpha/\epsilon \ll 1$; otherwise the quadratic enhancement may vanish. In Fig. 8, we illustrate the QCR bound of interaction strength α with HO pointer and rotation coupling, and ϵ varies from 0.1 to 0.01. As is shown in Fig. 8, when the post-selection angle ϵ is small enough to violate the approximate condition $M_w \ll 1$, the Heisenberg-like limit would vanish. Thus, the condition $M_w \ll 1$ should be strictly fulfilled in our scheme.

APPENDIX B: DERIVATION OF QFI FOR MONITORING QUBITS WITH A WEAK MEASUREMENT SCHEME

As is elucidated in the main text, the ancillary pointer is adopted to monitor the qubit via a weak interaction procedure

$\hat{U} \approx 1 - i\alpha\hat{\sigma}_z \otimes \hat{\Omega}$. Then the measurement information of the Pauli operator $\hat{\sigma}_z$ on the qubit is transferred to the pointer shift of the ancillas via a translation operator $\hat{\Omega}$, and the final state of the whole system is

$$|\Psi_f\rangle = \cos \frac{\theta}{2} |0\rangle |\psi_+\rangle + e^{i\phi} \sin \frac{\theta}{2} |1\rangle |\psi_-\rangle, \quad (\text{B1})$$

where $|\psi_+\rangle = \exp(-i\alpha\hat{\Omega})|\psi_i\rangle$ and $|\psi_-\rangle = \exp(i\alpha\hat{\Omega})|\psi_i\rangle$. Taking a partial trace on the state $|\Psi_f\rangle$, the final pointer can be calculated as a mixed state

$$\begin{aligned} \hat{\rho}_f &= \text{Tr}_{\text{qubit}}(|\Psi_f\rangle\langle\Psi_f|) \\ &= \cos^2 \frac{\theta}{2} |\psi_+\rangle\langle\psi_+| + \sin^2 \frac{\theta}{2} |\psi_-\rangle\langle\psi_-|. \end{aligned} \quad (\text{B2})$$

The QFI of parameter θ on state $\hat{\rho}_f$ is given by

$$\mathcal{Q}(\theta) = \text{Tr}(\hat{\rho}_f \hat{L}_\theta^2), \quad (\text{B3})$$

where \hat{L}_θ is the symmetric logarithmic derivative (SLD) for parameter θ , and it is governed by the relation [29]

$$\hat{\rho}_f \hat{L}_\theta + \hat{L}_\theta \hat{\rho}_f = 2\partial_\theta \hat{\rho}_f. \quad (\text{B4})$$

To calculate the QFI in Eq. (B3), we construct a set of eigenkets $\mathcal{S} = \{|e_1\rangle, |e_2\rangle, \dots, |e_n\rangle\}$ on the Hilbert space of state $\hat{\rho}_f$, where $n = \dim(\hat{\rho}_f)$ is the dimension of this Hilbert space, and the eigenkets $|e_1\rangle, |e_2\rangle$ are constructed as

$$\begin{aligned} |e_1\rangle &= \frac{1}{\sqrt{2(1+\delta)}} (|\psi_+\rangle + |\psi_-\rangle), \\ |e_2\rangle &= \frac{1}{\sqrt{2(1-\delta)}} (|\psi_+\rangle - |\psi_-\rangle), \end{aligned} \quad (\text{B5})$$

where $\delta = \text{Re}\langle\psi_+|\psi_-\rangle = \text{Re}\langle\psi_i|e^{i2\alpha\hat{\Omega}}|\psi_i\rangle \approx 1 - 2\alpha^2\langle\hat{\Omega}^2\rangle_i$. Then the final pointer state can be rewritten as

$$\begin{aligned} \hat{\rho}_f &= \frac{1+\delta}{2} |e_1\rangle\langle e_1| + \frac{1-\delta}{2} |e_2\rangle\langle e_2| \\ &\quad \times \langle e_2| + \frac{\sqrt{1-\delta^2}}{2} \cos \theta (|e_1\rangle\langle e_2| + |e_2\rangle\langle e_1|), \end{aligned} \quad (\text{B6})$$

and its partial derivative of θ is

$$\partial_\theta \hat{\rho}_f = -\frac{\sqrt{1-\delta^2}}{2} \sin \theta (|e_1\rangle\langle e_2| + |e_2\rangle\langle e_1|). \quad (\text{B7})$$

Combining with Eqs. (B4) and (B6), we have four equations about the matrix entries of SLD \hat{L}_θ :

$$\begin{cases} 2\langle e_1|\partial_\theta \hat{\rho}_f|e_1\rangle = (1+\delta)\langle e_1|\hat{L}_\theta|e_1\rangle + \frac{\sqrt{1-\delta^2}}{2} \cos \theta (\langle e_2|\hat{L}_\theta|e_1\rangle + \langle e_1|\hat{L}_\theta|e_2\rangle) = 0 \\ 2\langle e_2|\partial_\theta \hat{\rho}_f|e_2\rangle = (1-\delta)\langle e_2|\hat{L}_\theta|e_2\rangle + \frac{\sqrt{1-\delta^2}}{2} \cos \theta (\langle e_1|\hat{L}_\theta|e_2\rangle + \langle e_2|\hat{L}_\theta|e_1\rangle) = 0 \\ 2\langle e_1|\partial_\theta \hat{\rho}_f|e_2\rangle = \langle e_1|\hat{L}_\theta|e_2\rangle + \frac{\sqrt{1-\delta^2}}{2} \cos \theta (\langle e_2|\hat{L}_\theta|e_2\rangle + \langle e_1|\hat{L}_\theta|e_1\rangle) = -\sqrt{1-\delta^2} \sin \theta \\ 2\langle e_2|\partial_\theta \hat{\rho}_f|e_1\rangle = \langle e_2|\hat{L}_\theta|e_1\rangle + \frac{\sqrt{1-\delta^2}}{2} \cos \theta (\langle e_1|\hat{L}_\theta|e_1\rangle + \langle e_2|\hat{L}_\theta|e_2\rangle) = -\sqrt{1-\delta^2} \sin \theta \end{cases} \quad (\text{B8})$$

from which we can calculate four matrix entries of SLD \hat{L}_θ :

$$\begin{aligned} \langle e_1|\hat{L}_\theta|e_1\rangle &= (1-\delta) \cot \theta, \\ \langle e_2|\hat{L}_\theta|e_2\rangle &= (1+\delta) \cot \theta, \\ \langle e_1|\hat{L}_\theta|e_2\rangle &= \langle e_2|\hat{L}_\theta|e_1\rangle = -\sqrt{1-\delta^2} \csc \theta. \end{aligned} \quad (\text{B9})$$

The expression of QFI in Eq. (B3) can be calculated by

$$\begin{aligned} \mathcal{Q}(\theta) &= \text{Tr}(\hat{\rho}_f \hat{L}_\theta^2) = \text{Tr}(\hat{L}_\theta \partial_\theta \hat{\rho}_f) = \sum_{|e_x\rangle \in \mathcal{S}} \langle e_x|\hat{L}_\theta \partial_\theta \hat{\rho}_f|e_x\rangle \\ &= -\frac{\sqrt{1-\delta^2}}{2} \sin \theta (\langle e_2|\hat{L}_\theta|e_1\rangle + \langle e_1|\hat{L}_\theta|e_2\rangle). \end{aligned} \quad (\text{B10})$$

Combining with Eq. (B9), the QFI can be calculated finally as

$$\mathcal{Q}(\theta) = 1 - \delta^2 = 1 - (\text{Re}\langle\psi_+|\psi_-\rangle)^2 \approx 4\alpha^2\langle\hat{\Omega}^2\rangle_i, \quad (\text{B11})$$

where $\langle\hat{\Omega}^2\rangle_i = \langle\psi_i|\hat{\Omega}^2|\psi_i\rangle$ is the secondary moment of the coupling operator $\hat{\Omega}$ on the initial pointer state.

APPENDIX C: GENERATION METHOD OF HG BEAMS AND EXPERIMENTAL RESULTS

Traditionally, a mode cleaner cavity is necessary for generating high-order HG beams [48,49]. However, a mode cleaner cavity is usually difficult to set up and control in experiments. In this work, we generate the high-order HG beams by an SLM and 4f spatial filter system [30], which is easier to implement in experiments.

In this scheme, the light beam from a 780 nm DBR laser was expanded to a 8.6-mm-width Gaussian beam by a fiber coupler. The complex amplitude of expanded Gaussian beam is denoted as $A_{\text{in}}(x, y) \exp[i\phi_{\text{in}}(x, y)]$. Then, inputting this light into a SLM, where the phase map $H(x, y)$ is displayed, the output amplitude of the SLM can be denoted as

$$S(x, y) = A_{\text{in}}(x, y) \exp[i\phi_{\text{in}}(x, y) + iH(x, y)]. \quad (\text{C1})$$

Here we denote the relative phase as $\phi_r = \phi_{\text{out}} - \phi_{\text{in}} + \phi_g$, where ϕ_g is the grating phase, and the relative amplitude is $A_r = A_{\text{out}}/A_{\text{in}}$. To filter the target light, we let

$$H(x, y) = f(A_r) \sin(\phi_r). \quad (\text{C2})$$

This is based on the Bessel expansion formula

$$\exp[i f(a) \sin(\phi)] = \sum_{q=-\infty}^{\infty} J_q[f(a)] \exp(iq\phi), \quad (\text{C3})$$


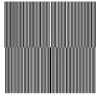
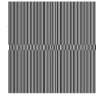
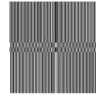
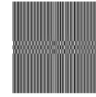

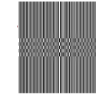
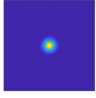






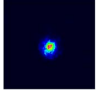
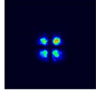
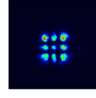
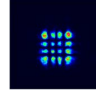
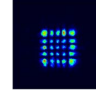
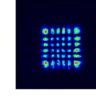
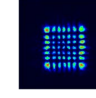
where $J_q[\cdot]$ is the q th-order Bessel function. Thus, the amplitude of the first-order diffraction beam is $A_{\text{in}} \cdot J_1[f(A_r)] \exp(i\phi_{\text{out}})$. The mapping function $f(\cdot)$ can be easily derived as

$$f(A_r) = J_1^{-1}(A_r), \quad (\text{C4})$$

where $J_1^{-1}(A_r)$ is the inverse function of the first-order Bessel function.

By employing a 4f spatial filter system with an aperture at the first-order diffraction point, we can generate any target beam amplitude $T(x, y) = A_{\text{out}} \exp(i\phi_{\text{out}})$ with the displayed

Table 3. Experimental Results of Generated HG Beams

HG Mode	HG00	HG11	HG22	HG33	HG44	HG55	HG66
Phase map							
Simulation							
Experiment							
Purity	97.87%	94.91%	93.76%	92.54%	90.17%	88.24%	86.75%

phase map $H(x, y) = J_1^{-1}(A_r) \sin(\phi_r)$ on the SLM. Here we illustrate the experimentally generated results of HG00 to HG66 beams and calculate the corresponding purity in the above table (Table 3).

APPENDIX D: IMPLEMENTATION OF PROJECTIVE MEASUREMENT

In our experimental scheme, the rotation signal was finally detected by projective measurement [17]. Suppose that the input light field on the SLM is $g(x, y)$, and the modulation light field on the SLM is $h(x, y)$ (the modulation method is same as the generation method of HG beams). The input field and the modulation field are simply combined as $g(x, y)h(x, y)$ on the SLM, and a Fourier lens transfers this field to

$$\begin{aligned} f(u, v) &= \mathcal{F}[g(x, y)h(x, y)] \\ &= \iint_{-\infty}^{+\infty} g(x, y)h(x, y) \exp[-i2\pi(xu + yv)] dx dy, \end{aligned} \quad (\text{D1})$$

which is spatially filtered by an SMF coupled to an APD, and the coupling efficiency into the fiber is given as

$$\eta \propto \left| \iint_{-\infty}^{+\infty} f(u, v) \exp\left(\frac{u^2 + v^2}{w_f^2}\right) du dv \right|^2, \quad (\text{D2})$$

where w_f is the field width of the fiber mode. In our experiment, $w_f = 4.6 \mu\text{m}$, which is much smaller than the features of $f(u, v)$. (The focal length of the Fourier lens is 10 cm, which transfers the waist width of the $500 \mu\text{m}$ HG00 beam to nearly $50 \mu\text{m}$.) Therefore, we have $\iint f(u, v) \exp[(u^2 + v^2)/w_f^2] du dv \approx \iint f(0, 0) \exp[(u^2 + v^2)/w_f^2] du dv$, which leads to

$$\eta \propto |f(0, 0)|^2 = \left| \iint_{-\infty}^{+\infty} g(x, y)h(x, y) dx dy \right|^2 = |\langle b^* | g \rangle|^2. \quad (\text{D3})$$

From Eq. (D3), we know that the detected intensity of the APD directly reflected the projective probability of state $|g\rangle$ on state $|b^*\rangle$ because the amplitude of the mn -order HG beam is real, i.e., $|u_{mn}(z)| = |u_{mn}^*(z)|$. By modulating $|\psi_l\rangle$ on the SLM, the detection probability of the APD is

$$P = |\langle \psi_l | \psi_f \rangle|^2 \approx (2mn + m + n)(\cot \epsilon)^2 \alpha^2. \quad (\text{D4})$$

In a practical system, the precision limit is given by the classical Cramér–Rao (CCR) bound [39,50] $\delta \hat{\alpha}^2 \geq 1/N \mathcal{F}(\alpha)$, where

$$\begin{aligned} \mathcal{F}(\alpha) &= \frac{1}{P} \left(\frac{\partial P}{\partial \alpha} \right)^2 + \frac{1}{1-P} \left[\frac{\partial(1-P)}{\partial \alpha} \right]^2 \\ &\approx 4(2mn + m + n)(\cot \epsilon)^2 \end{aligned} \quad (\text{D5})$$

is the classical Fisher information of our projection measurement. Thus, the minimum practical detectable rotation α given by the CCR bound is

$$\alpha_{\min}^{\text{CCR}} = \frac{1}{\sqrt{2mn + m + n} |\cot \epsilon| \sqrt{N}}, \quad (\text{D6})$$

which determines that $\alpha_{\min}^{\text{CCR}} = \alpha_{\min}^{\text{QCR}}$. In other words, the significant enhancement of measurement precision can be achieved in a practical optical system without involving any quantum resources.

Funding. National Natural Science Foundation of China (61631014, 61671287, 61901258, 62071298); State Key Laboratory of Advanced Optical Communication Systems and Networks.

Acknowledgment. We thank Lijian Zhang and Kui Liu for the helpful discussions.

Disclosures. The authors declare no conflicts of interest.

Data Availability. Data underlying the results presented in this paper are not publicly available at this time but may be obtained from the authors upon reasonable request.

REFERENCES

1. J. K. Stockton, K. Takase, and M. A. Kasevich, “Absolute geodetic rotation measurement using atom interferometry,” *Phys. Rev. Lett.* **107**, 133001 (2011).
2. M. Padgett and R. Bowman, “Tweezers with a twist,” *Nat. Photonics* **5**, 343–348 (2011).
3. J. Courtial, D. A. Robertson, K. Dholakia, L. Allen, and M. J. Padgett, “Rotational frequency shift of a light beam,” *Phys. Rev. Lett.* **81**, 4828–4830 (1998).

4. M. P. J. Lavery, F. C. Speirits, S. M. Barnett, and M. J. Padgett, "Detection of a spinning object using light's orbital angular momentum," *Science* **341**, 537–540 (2013).
5. Z. Zhang, L. Cen, J. Zhang, J. Hu, F. Wang, and Y. Zhao, "Rotation velocity detection with orbital angular momentum light spot completely deviated out of the rotation center," *Opt. Express* **28**, 6859–6867 (2020).
6. S. Shi, D.-S. Ding, Z.-Y. Zhou, Y. Li, W. Zhang, and B.-S. Shi, "Magnetic-field-induced rotation of light with orbital angular momentum," *Appl. Phys. Lett.* **106**, 261110 (2015).
7. F. Pampaloni and J. Enderlein, "Gaussian, Hermite-Gaussian, and Laguerre-Gaussian beams: a primer," arXiv:physics/0410021 (2004).
8. L. Allen, M. W. Beijersbergen, R. J. C. Spreeuw, and J. P. Woerdman, "Orbital angular momentum of light and the transformation of Laguerre-Gaussian laser modes," *Phys. Rev. A* **45**, 8185–8189 (1992).
9. R. Fickler, R. Lapkiewicz, W. N. Plick, M. Krenn, C. Schaeff, S. Ramelow, and A. Zeilinger, "Quantum entanglement of high angular momenta," *Science* **338**, 640–643 (2012).
10. A. K. Jha, G. S. Agarwal, and R. W. Boyd, "Supersensitive measurement of angular displacements using entangled photons," *Phys. Rev. A* **83**, 053829 (2011).
11. F. Bouchard, P. de la Hoz, G. Björk, R. W. Boyd, M. Grassl, Z. Hradil, E. Karimi, A. B. Klimov, G. Leuchs, J. Řeháček, and L. L. Sánchez-Soto, "Quantum metrology at the limit with extremal majorana constellations," *Optica* **4**, 1429–1432 (2017).
12. V. D'Ambrosio, N. Spagnolo, L. Del Re, S. Slussarenko, Y. Li, L. C. Kwek, L. Marrucci, S. P. Walborn, L. Aolita, and F. Sciarrino, "Photonic polarization gears for ultra-sensitive angular measurements," *Nat. Commun.* **4**, 2432 (2013).
13. I. Afek, O. Ambar, and Y. Silberberg, "High-noon states by mixing quantum and classical light," *Science* **328**, 879–881 (2010).
14. G. Y. Xiang, B. L. Higgins, D. W. Berry, H. M. Wiseman, and G. J. Pryde, "Entanglement-enhanced measurement of a completely unknown optical phase," *Nat. Photonics* **5**, 43–47 (2011).
15. B. L. Higgins, D. W. Berry, S. D. Bartlett, H. M. Wiseman, and G. J. Pryde, "Entanglement-free Heisenberg-limited phase estimation," *Nature* **450**, 393–396 (2007).
16. R. Barboza, A. Babazadeh, L. Marrucci, F. Cardano, C. de Lisio, and V. D'Ambrosio, "Ultra-sensitive measurement of transverse displacements with linear photonic gears," *Nat. Commun.* **13**, 1080 (2022).
17. O. S. Magaña Loaiza, M. Mirhosseini, B. Rodenburg, and R. W. Boyd, "Amplification of angular rotations using weak measurements," *Phys. Rev. Lett.* **112**, 200401 (2014).
18. V. Delaubert, N. Treps, M. Lassen, C. C. Harb, C. Fabre, P. K. Lam, and H.-A. Bachor, "tem₁₀ homodyne detection as an optimal small-displacement and tilt-measurement scheme," *Phys. Rev. A* **74**, 053823 (2006).
19. H. Sun, K. Liu, Z. Liu, P. Guo, J. Zhang, and J. Gao, "Small-displacement measurements using high-order Hermite-Gauss modes," *Appl. Phys. Lett.* **104**, 121908 (2014).
20. A. Holevo, *Unbiased Measurements* (Edizioni della Normale, 2011), pp. 219–264.
21. C. Rosales-Guzmán, N. Hermosa, A. Belmonte, and J. P. Torres, "Experimental detection of transverse particle movement with structured light," *Sci. Rep.* **3**, 2815 (2013).
22. N. Uribe-Patarroyo, A. Fraine, D. S. Simon, O. Minaeva, and A. V. Sergienko, "Object identification using correlated orbital angular momentum states," *Phys. Rev. Lett.* **110**, 043601 (2013).
23. Y. Aharonov, D. Z. Albert, and L. Vaidman, "How the result of a measurement of a component of the spin of a spin-1/2 particle can turn out to be 100," *Phys. Rev. Lett.* **60**, 1351–1354 (1988).
24. R. Jozsa, "Complex weak values in quantum measurement," *Phys. Rev. A* **76**, 044103 (2007).
25. K. Matsumoto, "A new approach to the Cramér-Rao-type bound of the pure-state model," *J. Phys. A* **35**, 3111–3123 (2002).
26. R. Demkowicz-Dobrzański, M. Jarzyna, and J. Kołodyński, "Chapter 4 - Quantum limits in optical interferometry," *Prog. Opt.* **60**, 345–435 (2015).
27. I. Kimel and L. R. Elias, "Relations between Hermite and Laguerre Gaussian modes," *IEEE J. Quantum Electron.* **29**, 2562–2567 (1993).
28. G. Nienhuis, "Analogies between optical and quantum mechanical angular momentum," *Philos. Trans. R. Soc. A* **375**, 20150443 (2017).
29. J. Liu, H. Yuan, X.-M. Lu, and X. Wang, "Quantum fisher information matrix and multiparameter estimation," *J. Phys. A: Math. Theor.* **53**, 023001 (2019).
30. T. W. Clark, R. F. Offer, S. Franke-Arnold, A. S. Arnold, and N. Radwell, "Comparison of beam generation techniques using a phase only spatial light modulator," *Opt. Express* **24**, 6249–6264 (2016).
31. O. Hosten and P. Kwiat, "Observation of the spin Hall effect of light via weak measurements," *Science* **319**, 787–790 (2008).
32. P. B. Dixon, D. J. Starling, A. N. Jordan, and J. C. Howell, "Ultrasensitive beam deflection measurement via interferometric weak value amplification," *Phys. Rev. Lett.* **102**, 173601 (2009).
33. M. Hallaji, A. Feizpour, G. Dmochowski, J. Sinclair, and A. Steinberg, "Weak-value amplification of the nonlinear effect of a single photon," *Nat. Phys.* **13**, 540–544 (2017).
34. H. Li, J.-Z. Huang, Y. Yu, Y. Li, C. Fang, and G. Zeng, "High-precision temperature measurement based on weak measurement using nematic liquid crystals," *Appl. Phys. Lett.* **112**, 231901 (2018).
35. C. Fang, J.-Z. Huang, and G. Zeng, "Robust interferometry against imperfections based on weak value amplification," *Phys. Rev. A* **97**, 063818 (2018).
36. L. Xu, Z. Liu, and L. Zhang, "Weak-measurement-enhanced metrology in the presence of ccd noise and saturation," in *Frontiers in Optics/Laser Science* (Optica Publishing Group, 2018), paper JW4A.126.
37. L. Xu, Z. Liu, A. Datta, G. C. Knee, J. S. Lundeen, Y.-Q. Lu, and L. Zhang, "Approaching quantum-limited metrology with imperfect detectors by using weak-value amplification," *Phys. Rev. Lett.* **125**, 080501 (2020).
38. A. Sone and P. Cappellaro, "Hamiltonian identifiability assisted by a single-probe measurement," *Phys. Rev. A* **95**, 022335 (2017).
39. C. Fang, B. Xia, J. Huang, T. Xiao, Y. Yu, H. Li, and G. Zeng, "Hamiltonian estimation based on adaptive weak value amplification," *J. Phys. B* **54**, 075501 (2021).
40. M. Genovese, "Experimental quantum enhanced optical interferometry," *AVS Quantum Sci.* **3**, 044702 (2021).
41. Z. K. Mineev, S. O. Mundhada, S. Shankar, P. Reinhold, R. Gutiérrez-Jáuregui, R. J. Schoelkopf, M. Mirrahimi, H. J. Carmichael, and M. H. Devoret, "To catch and reverse a quantum jump mid-flight," *Nature* **570**, 200–204 (2019).
42. M. Hays, V. Fatemi, K. Serniak, D. Bouman, S. Diamond, G. de Lange, P. Krogstrup, J. Nygård, A. Geresdi, and M. H. Devoret, "Continuous monitoring of a trapped superconducting spin," *Nat. Phys.* **16**, 1103–1107 (2020).
43. M. D. LaHaye, J. Suh, P. M. Echternach, K. C. Schwab, and M. L. Roukes, "Nanomechanical measurements of a superconducting qubit," *Nature* **459**, 960–964 (2009).
44. M. Kjaergaard, M. E. Schwartz, J. Braumüller, P. Krantz, J. I.-J. Wang, S. Gustavsson, and W. D. Oliver, "Superconducting qubits: current state of play," *Annu. Rev. Condens. Matter Phys.* **11**, 369–395 (2020).
45. A. D. O'Connell, M. Hofheinz, M. Ansmann, R. C. Bialczak, M. Lenander, E. Lucero, M. Neeley, D. Sank, H. Wang, M. Weides, J. Wenner, J. M. Martinis, and A. N. Cleland, "Quantum ground state and single-phonon control of a mechanical resonator," *Nature* **464**, 697–703 (2010).
46. B. Pepper, V. Ghobadi, E. Jeffrey, C. Simon, and D. Bouwmeester, "Optomechanical superpositions via nested interferometry," *Phys. Rev. Lett.* **109**, 023601 (2012).
47. K. C. Balram, M. I. Davanço, J. D. Song, and K. Srinivasan, "Coherent coupling between radiofrequency, optical and acoustic waves in piezo-optomechanical circuits," *Nat. Photonics* **10**, 346–352 (2016).
48. W. Kong, A. Sugita, and T. Taira, "Generation of Hermite-Gaussian modes and vortex arrays based on two-dimensional gain distribution controlled microchip laser," *Opt. Lett.* **37**, 2661–2663 (2012).
49. S.-C. Chu, Y.-T. Chen, K.-F. Tsai, and K. Otsuka, "Generation of high-order Hermite-Gaussian modes in end-pumped solid-state lasers for square vortex array laser beam generation," *Opt. Express* **20**, 7128–7141 (2012).
50. B. Xia, J. Huang, C. Fang, H. Li, and G. Zeng, "High-precision multiparameter weak measurement with Hermite-Gaussian pointer," *Phys. Rev. Appl.* **13**, 034023 (2020).